Available online at www.sciencedirect.com

ScienceDirect

journal homepage: www.elsevier.com/locate/he

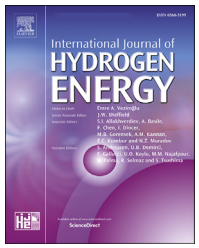

Compressive behaviour of thin catalyst layers. Part II - Model development and validation

Ali Malekian [a], Sina Salari [a], Mickey Tam [b], Ned Djilali [c], Majid Bahrami [a,*]

[a] Laboratory for Alternative Energy Conversion (LAEC), School of Mechatronic Systems Engineering, Simon Fraser University, Surrey, BC V3T 0A3, Canada

[b] Automotive Fuel Cell Cooperation, 9000 Glenlyon Parkway, Burnaby, BC V5J 5J8, Canada

[c] Department of Mechanical Engineering and Institute for Integrated Energy Systems, University of Victoria, Victoria V8P 5C2, BC, Canada

ARTICLE INFO

Article history:
Received 16 November 2018
Received in revised form
8 April 2019
Accepted 15 April 2019
Available online 4 June 2019

Keywords:
Catalyst layer
Compression
Analytical modeling
Deformation
Stress strain
Module of elasticity

ABSTRACT

In the second part of this study, a new analytical model for catalyst layers (CLs) compression is developed using effective medium theory, using a geometric "unit cell", to accurately predict the deformation of CLs under compression. Based on SEM images, a representative unit cell is proposed using microstructural properties of CL such as porosity, pore size distribution, and ionomer to carbon weight ratio (I/C) to simplify the random complex structure of CLs. Deformation of the ionomer film that covers carbon agglomerates is found to be the main deformation compared to other mechanisms such as Hertzian compliance of carbon particles and deformation of agglomerates. The present model is validated using the experimental results obtained for five different CL designs, presented in Part 1 of this study. The analytical model is capable of predicting the non-linear compressive behaviour of CLs with a reasonable accuracy since a continuous change of CL porosity is considered in the model. The proposed geometrical model has also been used for other properties of CL in our group and successfully predicted thermal conductivity and gas diffusivity of CL.

Introduction

Membrane Electrode Assembly (MEA) in Proton Exchange Membrane (PEM) fuel cells consist of a membrane, two catalyst layers (CLs), and two gas diffusion layers (GDLs) in the simplest form. All these layers tolerate numerous cyclic temperature, humidity, and pressure changes during the operation of PEM fuel cell which cause hygrothermal stresses in each layer [1]. The performance, life-time, and efficiency of fuel cell are affected by the change in properties of the MEA layers because of hygrothermal stresses [2–4]. Hence, mechanical properties of each layer should be modeled and validated experimentally to be able to predict the behaviour under different operating and loading conditions and over life time. CLs are one of the most important layers in PEM fuel cells since the main electrochemical reaction producing water and heat occurs in them. The first part of this study has focused on CL compressive behaviour experimentally [52]. In the second part, the focus is to analytically model behaviour of CL under uniaxial mechanical pressure to predict CL deformation.

* Corresponding author.
E-mail address: mbahrami@sfu.ca (M. Bahrami).

https://doi.org/10.1016/j.ijhydene.2019.04.135

Nomenclature

A_{CL}	CL sample area (mm^2)
a	Radius of aggregates (mm)
B	Material constant
d	Deformation (mm)
E	Young's modulus (MPa)
E'	Effective Young's modulus in Hertzian contact (MPa)
F	Force (N)
$N_{unit\ cell}$	Number of unit cells in one layer
n	Average number of contacts per spheres
P	Pressure (MPa)
R_c	Radius of carbon particle (mm)
R	Radius of ionomer shell (mm)
r	Radius of agglomerates (mm)
r_{pore}	Equivalent radius of pores (mm)
t	Thickness (mm)
$t_{ionomer}$	Thickness of ionomer around agglomerate (mm)
t_{CL0}	Initial thickness of catalyst layer (μm)
t_{CL-new}	New thickness of catalyst layer (μm)
V	Volume (mm^2)
Δt	Thickness change (μm)
ΔF	Force increment (N)
υ	Poisson's ratio
φ	Overlap angle
λ	A factor depending on the geometry and Poisson's ratio of material
$w_{I/C}$	Volume ratio of ionomer to carbon (mm^3/mm^3)
ξ	Overlapping parameter
β	Lamé's first parameter (MPa)
μ	Shear modulus (MPa)
γ_0	Euler's constant
ε	Porosity
ε_{new}	New porosity of CL
ε_0	Initial porosity of CL
ε_{arr}	Porosity of arrangement

Literature review

There are a number of experimental studies available in the literature with a focus on crack formation and initiation in CL. Among these studies, publications on mechanical properties of CLs by Fuel Cell System Development Div. at Toyota in Japan is notable [3,5–7]. However, there are very few publications on modeling mechanical properties of CLs [8,9].

Uchiyama et al. [10] measured static friction coefficient between micro-porous layer (MPL) and CL as a function of the clamping force which increased with clamping force (contact pressure). They found that at lower contact pressures, MEA deformed into wrinkle shapes but at higher contact pressures, bulging happens rather than wrinkling. The samples wrinkled by large in-plane swelling after buckling when swelling could not be restricted by the friction force from MPLs. Moreover, the results showed that, whether in air or in water, static friction coefficient increased as the contact pressure increased. In another study, Kai et al. [7] studied the effect of carbon fibers on CL crack formation. They reported that by increasing the space between carbon fibers, the CL bulged faster which resulted in crack formation. The experiments were conducted in various temperatures which suggested that the critical distance between fibers, beyond which the CL bulged and crack formed, became narrower as the temperature increased. Moreover, they investigated the effect of humidity cycles which caused the CL to deform plastically, bulge and crack. The results revealed that the MEA deformed significantly by swelling and residual deformation was observed under the dry condition, even for one humidity cycle.

Zenyuk et al. [9] developed a deterministic model in which two-dimensional surface profile (surface topology) of CL was an input. They studied the effect of interface of CL and MPL on the deformation and the amount of water that can be stored between two layers which resulted in deterioration of the PEM fuel cell performance. The developed model utilized two-dimensional surface profiles and computed local surface deformation and interfacial gap as a function of compression pressure. They found that a cracked interface between MPL and CL resulted in twice the interfacial gap compared to a crack-free interface at the same contact pressure. They also suggested that the contact resistance did not change for the two cases because the overall area of cracks was a low percentage of total sample area.

To the authors' best knowledge, there is no study on deformation of CLs under cyclic compression and no model has been developed to predict CL deformation. In this study, a new effective medium model, based on a geometrical "unit cell", is developed to analyze the deformation of CLs under compression. This method has been used to study compressive behaviour of other porous material, e.g. gas diffusion layer and aerogel blankets, in other studies as well [11–13]. The present model is compared with experimental results obtained in the Part I of this study [52] and shows reasonable agreement.

Microstructure modeling of CL

The proposed geometrical model simplifies the random and complicated microstructure of porous medium using unit cell approach. In this approach, a unit cell is considered as a geometrical representative of the entire medium. This method has been used in previous studies in Dr. Bahrami's group [12–15] and other publications [16–18]. It is assumed that the unit cell is repeated throughout the medium and contains all salient properties of the CL. Hence, the key factor in this approach is to develop a simple yet comprehensive geometrical model that can represent the microstructure of catalyst layer efficiently. The geometrical model adopted in this paper has been successfully used to accurately predict other properties of CLs, including: thermal conductivity [14] and gas diffusivity [15,19]. This versatility and simplicity attest to the capability of this powerful modeling platform and demonstrate its potential for further development and application for thin porous layers in other engineering applications.

Microstructure of CL

Catalyst layer is a complex random porous medium that consists of carbon particles, ionomer, and Pt particles supported on the carbon particles. Agglomerate is a cluster of carbon particles that are covered with ionomer film and also, they are connected throughout the CL medium. The pores of catalyst layer are often divided into two broad categories: i) primary pores (less than ~20 nm), which are between carbon particles within agglomerates [20,21]; and ii) secondary pores (20–300 nm), which are between the agglomerates and are usually bigger than primary pores. Fig. 1 shows the primary and secondary pores in a typical CL. In the present model, carbon particles are considered to be spherical, consistent with the literature [22–24]. The carbon particles bond and form the agglomerates. The properties of agglomerates such as the number of carbon particles in an agglomerate, their arrangement, and size are dependent on the fabrication process as well as the supplier [25]. In this model, the structure of CL is considered in two scales: i) structure within the agglomerate which consists of carbon particles with Pt particles on them; ii) structure of agglomerates that are connected together with secondary pores between them.

Geometrical model of agglomerates

There are generally two geometrical models in the literature for modeling CL properties: i) agglomerates are considered as spheres without overlap, i.e. touching at one point [27–32], ii) spheres with overlap which is our group's approach [14,15,19,33,34]. The papers from our group show that the models with overlap spheres have better agreement with experimental data for CL properties such as thermal conductivity and gas diffusivity. Also, CL structure modeled using spherical agglomerates without overlap have overestimated active surface area and gas diffusivity compared to the reconstructed CL geometry from FIB-SEM images [35]. Hence, overlapping spherical agglomerates are considered for the mechanical modeling in this study. Also, it is assumed that ionomer covers the agglomerates partially and blocks a portion of the primary pores within the agglomerates. The spherical agglomerates are considered to have a simple cubic (SC) arrangement to make it possible for modeling. A schematic of the proposed geometry is shown in Fig. 2.

Geometrical model within agglomerates

In this model, carbon particles within agglomerates are considered to be equally sized spherical particles, which is consistent with other studies [14,33,36]. The arrangement of carbon particles in the aggregates are considered to be face-centered cubic (FCC) since it features the closest arrangement to a randomly packed spheres with porosity (=0.26 [37]). It will be shown later that the carbon particles packing inside the agglomerates does not play an important role in the mechanical deformation model since the deformation of the carbon particles inside the agglomerates are negligible compared to deformation of the ionomer shell. Fig. 3a shows the unit cell used in this study which is the main element that makes up the CL microstructure shown in Fig. 2. As mentioned, the agglomerates have overlap that is described by an overlap angle, φ. Also, Fig. 3b shows the ionomer shell that covers and holds the agglomerate in the present unit cell geometry.

Geometrical calculation for unit cell

As it is drawn in Figs. 2 and 3, void volume between the overlapping agglomerates are the secondary pores of CL, whereas, the primary pores are the void volume between the spherical carbon particles. The overlapping parameter, ξ, is defined as the ratio of radius of agglomerate to radius of aggregate (i.e. $\xi = r/a$), which is related to the overlap angle, φ as it is shown in Fig. 3. These values are related to each other using Eqs. (1) and (2). The radius of aggregates, or size of unit cell (a), and radius of agglomerates (r) are calculated based on secondary pore sizes. The thickness of ionomer around agglomerates and the portion of blocked primary pores are calculated from pore size distribution (PSD) and porosity of CL

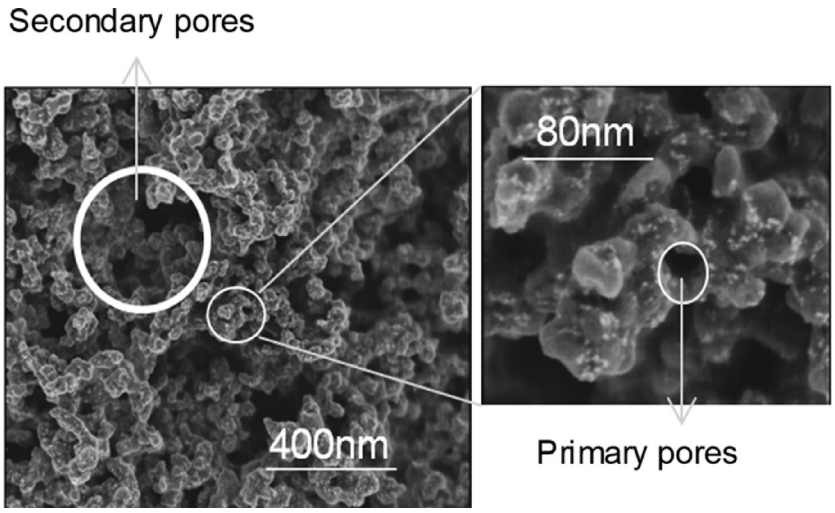

Fig. 1 – Primary and secondary pores in a CL [26].

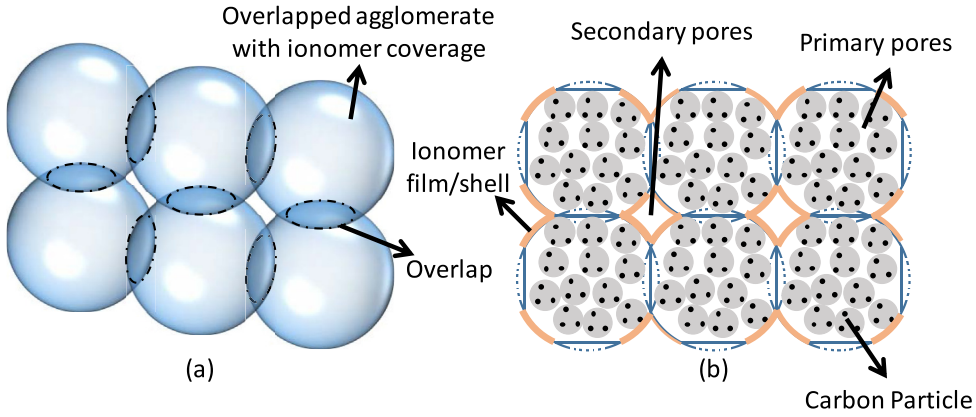

Fig. 2 – Schematic of simplified geometrical model of CL; a) overlapping agglomerates b) primary and secondary pores with carbon particles and ionomers.

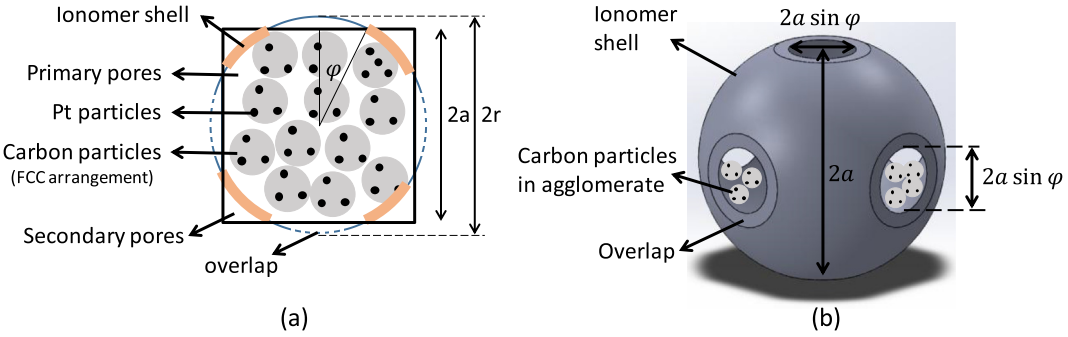

Fig. 3 – Unit cell of simplified geometry used in this study: (a) 2D view of an agglomerate, (b) geometry of ionomer shell around agglomerates (ionomer thickness is shown with exaggeration).

(ε_{CL}). More details of the calculations can be found in other papers published by Salari et al. [15,19].

$$\xi = r/a \tag{1}$$

$$\varphi = \cos^{-1}(1/\xi) \tag{2}$$

By considering FCC arrangement for carbon particles inside the agglomerates, the following equations for agglomerate porosity ($\varepsilon_{agglomerate}$), volume of agglomerates ($V_{agglomerate}$), porosity of catalyst layer (ε_{CL}) and overlapping parameter (ξ) can be written:

$$\varepsilon_{C-Pt} = \varepsilon_C \frac{\rho_{Pt}}{\rho_{Pt} + \rho_C \omega_{Pt/C}} \tag{3}$$

$$\varepsilon_{agglomerate} = \frac{\rho_{Pt}\rho_I \varepsilon_{C\text{-}Pt}(1-\varepsilon_{FCC}) + \rho_I(\rho_{Pt} + \rho_C\omega_{Pt/C})\varepsilon_{FCC}}{\rho_I(\rho_{Pt} + \rho_C\omega_{Pt/C}) + \rho_{Pt}\rho_C\omega_{I/C}(1-\varepsilon_{FCC})} \tag{4}$$

$$\varepsilon_{CL} = 1 - \frac{V_{agglomerate}(1-\varepsilon_{agglomerate})}{8a^3} \tag{5}$$

$$V_{agglomerate} = V_{sphere} - 6V_{overlap} = \frac{4}{3}\pi a^3(4.5\xi^2 - 2\xi^3 - 1.5) \tag{6}$$

$$\varepsilon_{CL} = 1 - \frac{\pi(1-\varepsilon_{agglomerate})(4.5\xi^2 - 2\xi^3 - 1.5)}{6} \tag{7}$$

$$\xi = \frac{3}{4} + \frac{9}{2\left(4\sqrt{16\Psi^2 - 6\Psi - 45} - 16\Psi + 3\right)^{\frac{1}{3}}} + \frac{1}{4}\left(4\sqrt{16\Psi^2 - 6\Psi - 45} - 16\Psi + 3\right)^{\frac{1}{3}} \tag{8}$$

$$\Psi = \frac{6(1-\varepsilon_{CL})}{\pi(1-\varepsilon_{agglomerate})} \tag{9}$$

where V_{C-Pt} is the total volume of carbon and platinum particles in the agglomerates including the pores inside carbon particle, ε_{C-Pt} is porosity of carbon and platinum particles combined, ρ_I, ρ_{Pt} and ρ_C are the densities of ionomer, platinum and carbon particles, respectively, $\omega_{I/C}$ and $\omega_{Pt/C}$ is the weight ratio of ionomer to carbon and platinum to carbon in CL, respectively, ε_C is the porosity of carbon support particles which is 0.29 as suggested by Voet and Aboytes [38], ε_{FCC} is the porosity of FCC arrangement which is 0.26 [37], $\varepsilon_{agglomerate}$ is the agglomerate porosity, ε_{CL} is the porosity of the proposed unit cell representing CL, Ψ is a dimensionless parameter used to simplify Eq. (8), V_{sphere} and $V_{overlap}$ is the volume of the sphere and one overlap at a side of sphere, respectively, as shown in Fig. 3.

As Bahrami et al. [39] suggested, an equivalent radius can be obtained from square root of the area (Eq. (11)) which is the area of the secondary pore (Eq. (10)) shown in Fig. 2. Using the

proposed geometry, one can find an equivalent pore radius for secondary pores between agglomerates as a function of size of unit cell (combining Eqs. (11)) & (10). Therefore, the unit cell size (i.e. a) can be found using Eq. (12) for different pore sizes obtained from PSD, which means unit cells in the simplified geometry have different sizes which is dependent on the sizes and volume percentage of pores in CL.

$$r_{pore} = 0.5\sqrt{A_{sp}} \tag{10}$$

$$A_{sp} = 4a^2 - A_{agglomerate} = 4a^2(1 - \tan\varphi) - (\pi - 4\varphi)r^2 \tag{11}$$

$$a = \frac{r_{pore}}{\sqrt{1 - \tan\varphi - \left(\frac{\pi}{4} - \varphi\right)\xi^2}} \tag{12}$$

where ξ can be found from Eq. (8) and φ can be found using Eq. (2), A_{sp} is area of the secondary pore, and r_{pore} is the radius of the pore. Knowing the unit cell geometry, one can find an average thickness of ionomer that covers the agglomerate using the following equations.

$$V_{carbon} = V_{agglomerate}(1 - \varepsilon_{FCC})(1 - \varepsilon_{C-Pt}) \tag{13}$$

$$V_{ionomer} = V_{carbon}\,\omega_{I/C} \tag{14}$$

$$t_{ionomer} = \frac{V_{ionomer}}{A_{agglomerate}} \tag{15}$$

$$A_{agglomerate} = 4\pi r^2 - 6 \times 2\pi r(r - a) \tag{16}$$

where $A_{agglomerate}$ is the total area covered by ionomer which is the area around the agglomerates, and $t_{ionomer}$ is the thickness of ionomer covering agglomerates. Using Eqs. (8), (10), and (15), one can build the geometrical model as shown in Figs. 2 and 3. Clearly, unit cell size has a distribution as the PSD measurements is used in this model.

Mechanical compression model

Fig. 3 shows a schematic of the proposed unit cell geometrical model used in this study. After developing an effective medium model for CL, its deformation due to mechanical pressure is obtained. Having the deformation of each unit cell, one can calculate the thickness change of the CL. To find the deformation of each unit cell, the following equations are used to find the applied force on each of them.

$$F_{tot} = PA_{CL} \tag{17}$$

$$F = \frac{F_{tot}}{N_{unit\ cell}} \tag{18}$$

where F_{tot} is the total force acting on CL, F is the force acting on each unit cell, $N_{unit\ cell}$ is the total number of unit cells in one layer, P is the pressure applied on the sample, and A_{CL} is the total (or nominal) surface area of CL sample under compression. The applied force is transferred through the ionomer to the particles inside the agglomerate, so particles are deformed and transfer the pressure to the ionomer. The applied force also changes the shape of the ionomer shell and the arrangement of particles inside agglomerate. Three different deformation modes are considered for each unit cell in this work: i) deformation due to Hertzian contact of carbon particles or compliance, ii) deformation of agglomerates as a packed bed of carbon particles (FCC arrangement), iii) deformation of ionomer shell, i.e. the spherical shell, shown in Fig. 3b.

Deformation due to Hertzian contact between carbon particles inside agglomerates

As described earlier, the applied force on the unit cell is transferred to the carbon particles within the agglomerates. The carbon particles deform which results in a compliance of the spherical particles. This deformation is because of the contact between the particles and can be calculated using Hertzian theory [40]. Considering the arrangement of carbon particles to be FCC, one can find the deformation using Eq. (19).

$$d_{FCC} = \frac{\sqrt{6}}{3}\left[\frac{F^2}{16E_c'^2 R_c}\right]^{1/3} \tag{19}$$

where d_{FCC} is the deformation of particles in FCC arrangements, F is the applied force on each agglomerate which is found based on the applied pressure, R_c is the radius of the carbon particles, and E_c' is the effective Young's modulus of the contact and can be calculated using $E_c' = \left(\frac{1-\nu_1}{E_1} + \frac{1-\nu_2}{E_2}\right)$.

Deformation of agglomerates

Other than the deformation of each particle in the agglomerate, the entire agglomerate can also deform which can be envisioned as a packed bed of spherical particles, contained within the ionomer film, Fig. 3b. The applied force changes the shape of agglomerates from sphere to an oval as schematically shown (exaggerated) in Fig. 4. The deformation of the agglomerate as a packed bed of spheres with an applied force on its top has been reported by Walton [41]. Eq. (20) shows the deformation of a random packing of spheres in which B depends on the material of the spheres inside the packing (i.e. carbon particles) and can be found from Eq. (21), F is the applied force on top of the packing, ε_{arr} is the porosity of the packing (i.e. $\varepsilon_{arr} = 0.26$ for FCC arrangement), and n is the average number of contacts per spheres in the packed bed.

$$d = \left[\frac{3\pi^2\, BF}{(1 - \varepsilon_{arr})n}\right]^{2/3} \tag{20}$$

$$B = \frac{1}{4\pi}\left(\frac{1}{\mu} + \frac{1}{\beta + \mu}\right); \quad \mu = \frac{E}{2(1+\nu)}; \quad \beta = \frac{E\nu}{(1+\nu)(1-2\nu)} \tag{21}$$

Deformation of ionomer shell

The applied force on the unit cell causes the ionomer shell to deform as well. Since each agglomerate is in contact with the one above it, the force applied to each of them is a point load from the top. Hence, the ionomer shell shown in Fig. 3b is subjected to a point force from the top. In this deformation mode, the carbon particles can move and slide freely on each

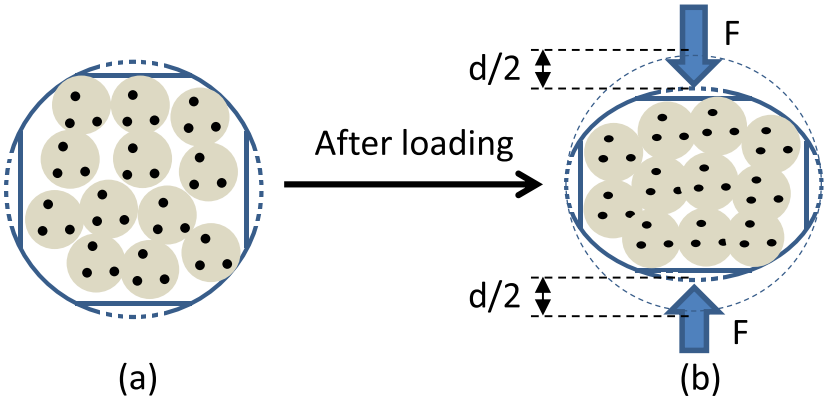

Fig. 4 – Compression of agglomerates as a packing of spheres. a) before loading, b) after loading (deformation exaggerated).

other, however, because they cannot penetrate in other particles, one can consider that they act as a fluid inside the spherical shell and by increasing the force on top, the internal pressure increases and do not let the ionomer shell to deform at the same rate. Since the size of carbon particles are small and there are so many of them inside the shell, it can be assumed that an almost "hydrostatic" pressure acting inside the shell. In other words, ionomer shell can be considered as a hollow spherical shell filled with fluid with a point load on top.

It is found that the overlapping parameter, ξ, is close to one which indicates that the size of the side holes compared to the shell diameter are small, hence the ionomer shell (Fig. 5a) can be considered as a whole spherical thin shell (Fig. 5b) which simplifies the deformation calculations as well. Fig. 5c shows the simplified geometry of ionomer shell as a spherical shell and its deformation under a point load. Koiter [42] considered a non-shallow hollow spherical shell loaded at vertex in spherical coordinates and found the normal deflection at the vertex, i.e. Eqs. (22) and (23). Also, Taber [43] considered a fluid-filled spherical shell under a point load, which has internal pressure, and found the deformation of the sphere as a function of the applied force on the vertex. Taber showed that the hollow sphere model (Koiter [42]) and fluid-filled sphere model (Taber [43]) have negligible difference at strains less than 15%. It has been shown that strain (at 5 MPa) is less than 15% after first compression cycle for CL samples in [52]. Also, because of relatively low strain of CLs, the forces on the sides of agglomerates have negligible effect on the deformation of ionomer shell. Therefore, Koiter's model [42] can be used in this study to calculate the deformation of the ionomer shell.

$$d = \frac{\sqrt{3(1-\nu^2)}}{4}\frac{F\,.\,r}{E_{ionomer}{t_{ionomer}}^2}\left[1+\frac{2(1+\nu)}{\pi\lambda^2}\left(\ln\lambda+\gamma_0-1+\frac{\ln 2}{2}\right)+\frac{4}{3\pi\lambda^2}\right] \quad (22)$$

$$\lambda^2 = \sqrt{3(1-\nu^2)}\,\frac{r}{t_{ionomer}} \quad (23)$$

where F is the applied force, $t_{ionomer}$ is the thickness of the shell, r is the radius of the spherical shell, λ is a factor depending on the geometry and Poisson's ratio of material, $\gamma_0 = 0.5772$ is the Euler's constant [42]. Using the above equations, one can find the deformation of the ionomer shell that covers the agglomerates.

Overall deformation of CL

Our experimental results [52] showed that the compressive behaviour of CL under compression had two regions and was not linear. The reason for this behaviour is the change in

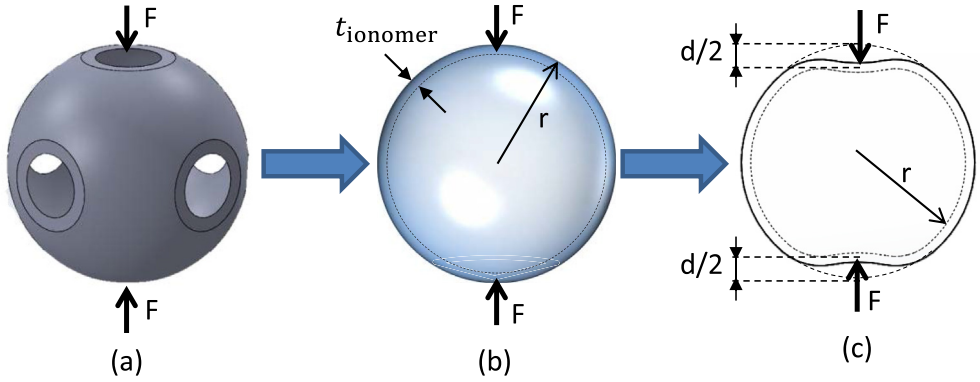

Fig. 5 – Steps in simplified geometrical model of ionomer shell to hollow spherical shell. a) the ionomer shell around the agglomerates, b) ionomer shell as a sphere around agglomerates, c) spherical shell deformation under point load F (exaggerated).

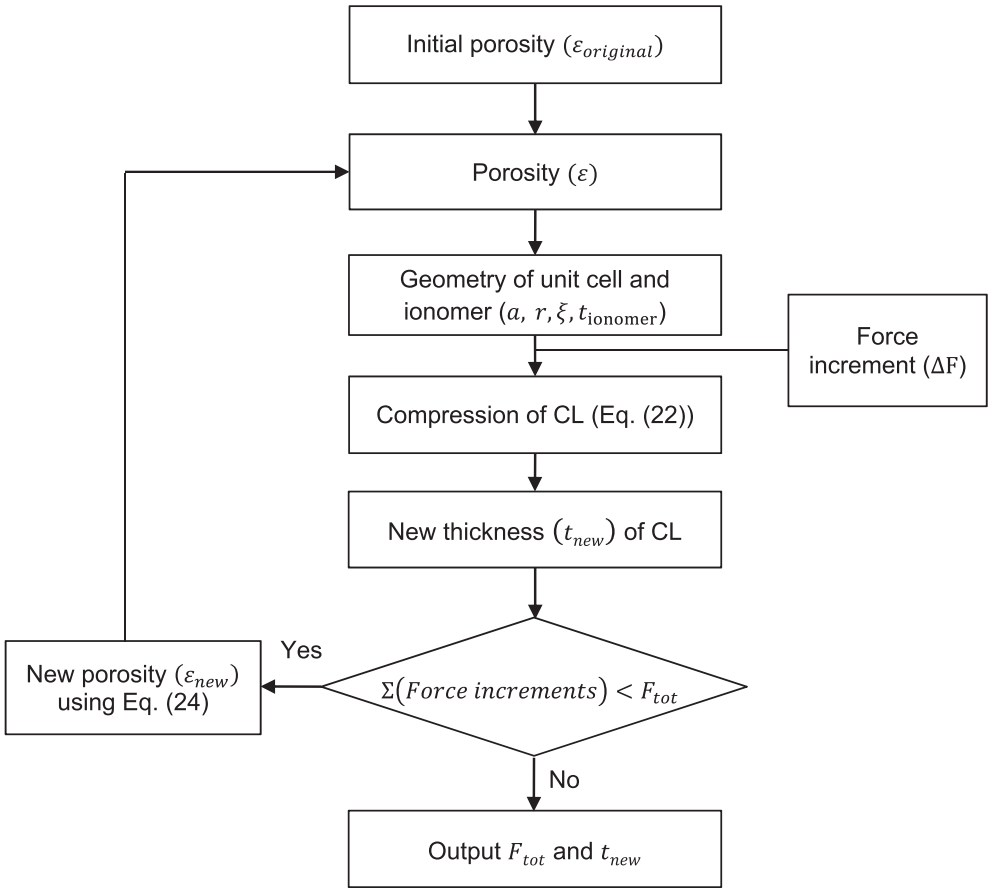

Fig. 6 – Algorithm of the proposed compression model for CLs (recursive model; at each step, a new geometry is created).

microstructure as CL undergoes compression. As a porous material gets compressed, contact nodes inside the layer increase, porosity decreases, and the material gets stiffer at higher pressures. This effect should be considered in the mechanical model because the porosity of the CL is continuously changing during compression. To account for this change, a recursive analytical model is developed in this paper. A new porosity is calculated based on new thickness after a small increment of force. In other words, it is considered that the force is applied in finite number of small steps (force increments steps) and after each step, new thickness and new porosity are calculated based on the given equations. Hence a new geometry is built for CL after each step. Eq. (24) is used to calculate CL porosity after deformation at any level, which has been widely used in the literature to model different properties of porous media [12,44–50]. This equation is based on the assumption that the solid volume inside the material does not change during compression. This is valid since the material is porous and the pores become smaller or even closed during compression and so the volume of solid material remains constant. Fig. 6 shows the flowchart of the CL compression model developed in this study. Obviously, as the number of steps in this model increases, the accuracy of the model increases and it's important to find the optimum number of steps. It is found that 500 steps are enough to get reasonable behaviour and beyond that the maximum strain changes less than 0.1%, which means that 500 steps are "infinity-enough" for our model.

Table 1 – Properties of different CLs used in this study (model inputs).

CL Design number	I/C ratio (gr/gr)	Densitometer porosity (%)	CL Thickness (μm)	Average size of agglomerates (nm) (calculated using PSD & model)	t_{ionomer} (nm) (calculated using PSD & model)	Mechanical properties of ionomer (measured using TMA)
Design 1	1.1	58.2	9.1	195	12.4	$E_{\text{ionomer}} = 93$ MPa$\nu =$ 0.3
Design 2	0.9	52.0	6.9	158	11.0	
Design 3	0.7	52.4	6.1	142	5.6	
Design 4	0.7	50.5	4.6	103	5.5	
Design 5	0.9	33.4	6.3	60	8.3	

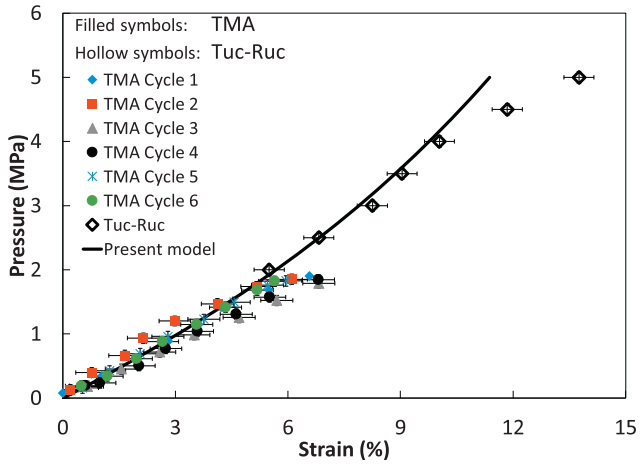

Fig. 7 – Comparison of the present mechanical model with experimental data for CL pressure vs strain (Design 1); colored symbols shows different cycles of CL compression up to 2 MPa using TMA.

$$\varepsilon_{new} = 1 - \frac{t_{CL0}}{t_{CL-new}}(1-\varepsilon_0) \quad or \quad \varepsilon_{new} = 1 - \frac{1}{1-\frac{\Delta t}{t_{CL0}}}(1-\varepsilon_0) \tag{24}$$

Under 5 MPa pressure, the deformation due to the Hertzian contact between carbon particles (Eq. (19)) is ~10^{-7} μm, deformation of the agglomerates as a packed bed (Eq. (20)) is ~10^{-6} μm, and the deformation of ionomer shell (Eq. (22)) is ~10^{-3} μm. This is due to the fact that ionomer has the lowest Young's modulus, 93 MPa compared to carbon particles Young's modulus of ~15 GPa [51]. Based on this order of magnitude analysis, the 9–14% strain at 5 MPa (experimental data collected in Part 1) is dominantly because of deformation of ionomer shell. It is considered that the carbon particles inside the agglomerates can slide and move freely on each other so that the ionomer shell deforms and Koiter [42] model can be used. To this end, only the deformation of the ionomer shell is considered for CL compression modeling in this study.

Results and discussion

The results of the proposed mechanical model are compared with the experimental results obtained in the Part 1 of this study [52]. The pore size distribution, I/C ratio, porosity, thickness, ink properties, and pressure are the inputs of the model which were measured for all the designs. Table 1 shows the properties of each design in this study. The pore size

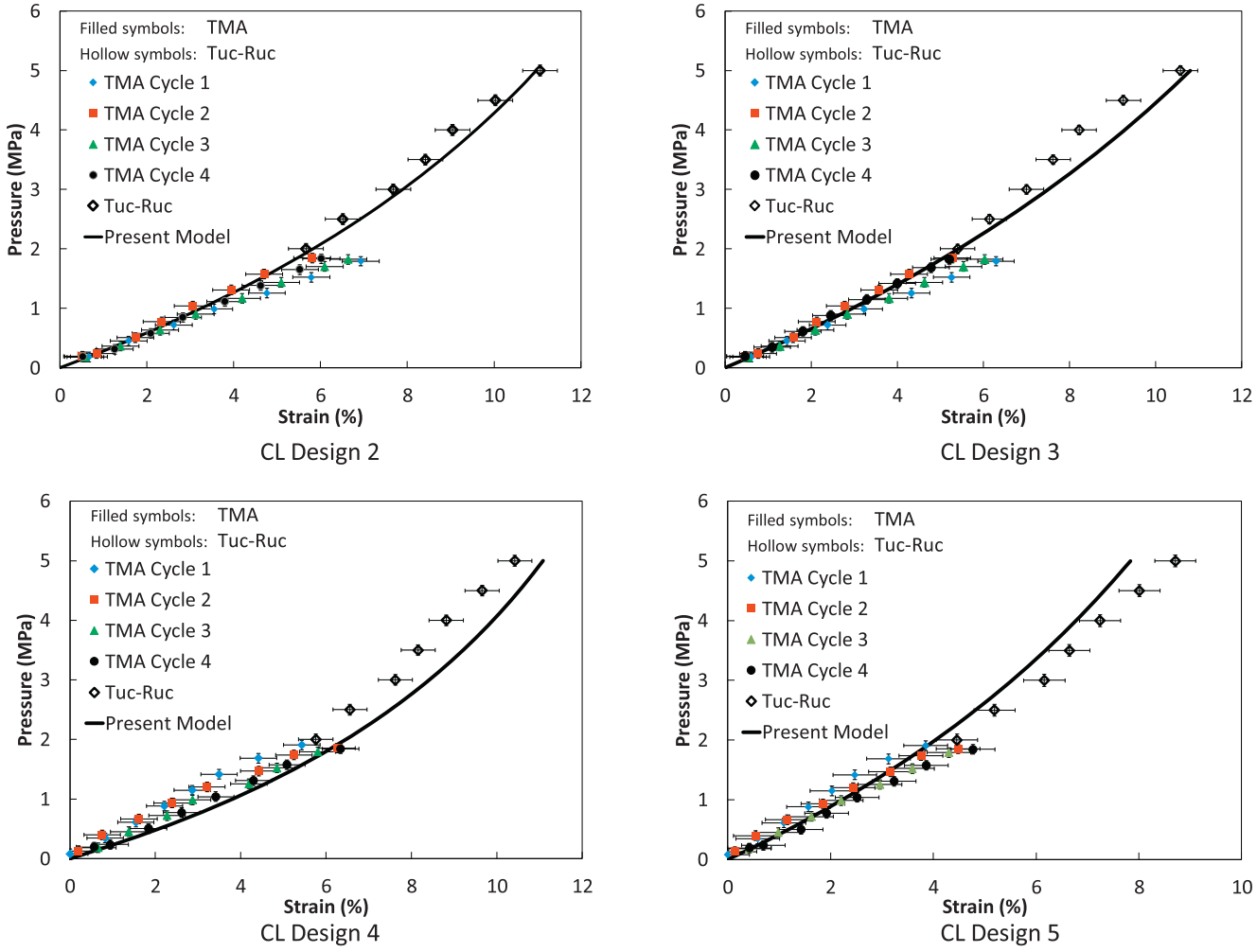

Fig. 8 – Comparison of the present mechanical model with experimental data for CL pressure vs strain (Design 2, 3, 4, and 5); colored symbols shows different cycles of CL compression up to 2 MPa using TMA.

distribution of each sample was measured using N_2 adsorption porosimetry [26] and it is used as input for geometrical model to calculate the average size of agglomerates and thickness of ionomer ($t_{ionomer}$) which are shown in Table 1.

Fig. 7 shows the comparison between the model and experimental pressure vs strain for CL Design 1. As shown in Fig. 7, the model captures the trend of the data and shows a reasonable agreement with the experimental results. It should be noted that the present model is non-linear as the change in porosity is considered in the model, even though the equations used for the deformation of ionomer is linear. Also note that the model is capable of predicting the non-linear behaviour of CLs over both regions that is explained in the Part 1 of this study [52]. The difference between the model and experimental data is relatively larger in the second region where the pressure is higher. This difference can be attributed to the hypothesis that some of the pores, thus the microstructure of the CL, are plastically deformed under higher pressure. More experimental studies are needed to better understand the behaviour at pressures between 2 to 5 MPa.

Similar behaviour is observed for other CL Designs. Fig. 8 shows a comparison of the present model and experiments for pressure vs strain of other CL Designs. The following can be concluded: i) the present model captures the trend of the experimental results and is able to predict the change in strain rate of the material with reasonable accuracy, ii) the model predicts the non-linear behaviour of the CL as the porosity continuously decreases. The average relative difference between the model and experimental data is 15%. The model over-estimates the strain at higher pressures for CL Designs 2 to 4 and under-estimates the strain at higher pressures for CL Design 1 and 5, which is within the uncertainty of the experimental results.

As shown in Figs. 7 and 8, the present model successfully captures the trend of the experimental results which makes it very useful for predicting compressive behaviour of CLs and other properties that are dependent on porosity or applied pressure. The proposed model can be used for other porous layers with similar microstructures since the core of the model considers the porosity change during compression and the inputs are salient geometrical parameters of a thin porous layer. The relative difference between the model and the experimental results are reasonable, and more importantly, the model captures the trends of the data.

Conclusion

In this study, an analytical model was developed for CL compression under uniaxial pressure using a unit cell approach. A unit cell was developed based on the microstructure of CL such that it could be a representative of the entire CL, meaning that it had the same microstructural properties of CL. The geometry of the unit cell was found using pore size distribution, ionomer to carbon weight ratio, and porosity. Three deformations: i) deformation due to Hertzian contact between carbon particles inside agglomerates, ii) deformation of agglomerates, and iii) deformation of the ionomer film were considered for the simplified geometry of the unit cell. Deformation of ionomer film around agglomerates was found to be the dominant deformation mode CL compression. The proposed analytical model is validated against experimental pressure vs strain data sets for five different CL designs with different ionomer to carbon weight ratios, porosities, thicknesses, and dry milling times. The model predicted the non-linear behaviour of CLs under compression with a reasonable discrepancy. The developed geometrical model has also been used in other studies in our group and successfully predicted other properties such as thermal conductivity and gas diffusivity of CLs. The main focus of this work has been on PEM fuel cell catalyst layers; however, the proposed modeling platform can be implemented to study mechanical properties of other porous thin layers, such as membrane and graphite sheets.

Acknowledgements

This research was supported by funding from the Natural Sciences and Engineering Research Council of Canada Collaborative Research and Development (Grant No. CRDPJ 452170-13) and Automotive Fuel Cell Corporation (AFCC), Canada. AFCC Structure, Properties & Performance Research Division is also acknowledged for their technical support.

REFERENCES

[1] Banan R, Zu J, Bazylak A. Humidity and temperature cycling effects on cracks and delaminations in PEMFCs. Fuel Cells 2015;15:327–36. https://doi.org/10.1002/fuce.201400118.

[2] Tang Y, Santare MH, Karlsson AM, Cleghorn S, Johnson WB. Stresses in proton exchange membranes due to hygro-thermal loading. J Fuel Cell Sci Technol 2006;3:119. https://doi.org/10.1115/1.2173666.

[3] Kai Y, Kitayama Y, Omiya M, Uchiyama T, Kato M. crack formation on membrane electrode assembly (MEA) under static and cyclic loadings. ASME 2012 10th Int. Conf. Fuel Cell Sci. Eng. Technol., Vol. 10; 2012. p. 143. https://doi.org/10.1115/FuelCell2012-91164.

[4] Kusoglu A, Karlsson AM, Santare MH, Cleghorn S, Johnson WB. Mechanical response of fuel cell membranes subjected to a hygro-thermal cycle. J Power Sources 2006;161:987–96. https://doi.org/10.1016/j.jpowsour.2006.05.020.

[5] Uchiyama T, Kato M, Ikogi Y, Yoshida T. Mechanical degradation mechanism of membrane electrode assemblies in buckling test under humidity cycles. J Fuel Cell Sci Technol 2012;9:061005. https://doi.org/10.1115/1.4007814.

[6] Uchiyama T, Kumei H, Yoshida T. Catalyst layer cracks by buckling deformation of membrane electrode assemblies under humidity cycles and mitigation methods. J Power Sources 2013;238:403–12. https://doi.org/10.1016/j.jpowsour.2013.04.026.

[7] Kai Y, Kitayama Y, Omiya M, Uchiyama T, Kumei H. In situ observation of deformation behavior of membrane electrode assembly under humidity cycles. J Fuel Cell Sci Technol 2014;11:051006. https://doi.org/10.1115/1.4028155.

[8] Ogawa S, Babu SK, Chung HT, Zelenay P, Padgett E, Muller DA, Kongkanand A, Litster S. Microstructural modeling of PEFC catalyst layer performance and durability. In: Meet. Abstr. The Electrochemical Society; 2017. p. 1374.

[9] Zenyuk IV, Kumbur EC, Litster S. Deterministic contact mechanics model applied to electrode interfaces in polymer

electrolyte fuel cells and interfacial water accumulation. J Power Sources 2013;241:379–87. https://doi.org/10.1016/j.jpowsour.2013.03.165.
[10] Uchiyama T, Kumei H, Yoshida T, Ishihara K. Static friction force between catalyst layer and micro porous layer and its effect on deformations of membrane electrode assemblies under swelling. J Power Sources 2014;272:522–30. https://doi.org/10.1016/j.jpowsour.2014.08.103.
[11] Norouzifard V, Bahrami M. Deformation of PEM fuel cell gas diffusion layers under compressive loading: an analytical approach. J Power Sources 2014;264:92–9. https://doi.org/10.1016/j.jpowsour.2014.04.057.
[12] Hoseini A, Malekian A, Bahrami M. Deformation and thermal resistance study of aerogel blanket insulation material under uniaxial compression. Energy Build 2016;130:228–37. https://doi.org/10.1016/j.enbuild.2016.08.053.
[13] Malekian A, McCague C, Salari S, Djilali N, Bahrami M. Compression of pem fuel cell gas diffusion layers: analytical model and experimental validation. In: 27th Int. Symp. Transp. Phenom.; 2016. Honolulu.
[14] Ahadi M, Putz A, Stumper J, Bahrami M. Thermal conductivity of catalyst layer of polymer electrolyte membrane fuel cells: Part 2 – analytical modeling. J Power Sources 2017;354:215–28. https://doi.org/10.1016/j.jpowsour.2017.03.100.
[15] Salari S, Stumper J, Bahrami M. Through plane gas diffusion of catalyst layer of PEMFC: bimodal unit cell modeling. In: 27th Inernational Symp. Transp. Phenom.; 2016. Honolulu.
[16] Xia Z, Zhou C, Yong Q, Wang X. On selection of repeated unit cell model and application of unified periodic boundary conditions in micro-mechanical analysis of composites. Int J Solids Struct 2006;43:266–78. https://doi.org/10.1016/J.IJSOLSTR.2005.03.055.
[17] Ganapathy D, Singh K, Phelan PE, Prasher R. An effective unit cell approach to compute the thermal conductivity of composites with cylindrical particles. J Heat Transf 2005;127:553. https://doi.org/10.1115/1.1915387.
[18] Botelho SJ, Banerjee R, Bazylak A. A unit-cell approach for determining the effective thermal conductivity of the polymer electrolyte membrane fuel cell microporous layer. Int J Heat Mass Transf 2015;89:809–16. https://doi.org/10.1016/j.ijheatmasstransfer.2015.05.116.
[19] Salari S, Stumper J, Bahrami M. Direct measurement and modeling relative gas diffusivity of PEMFC catalyst layers: the effect of ionomer to carbon ratio, operating temperature, porosity, and pore size distribution. Int J Hydrogen Energy 2018;43:16704–18. https://doi.org/10.1016/j.ijhydene.2018.07.035.
[20] Uchida M, Aoyama Y, Eda N, Ohta A. Investigation of the microstructure in the catalyst layer and effects of both perfluorosulfonate ionomer and PTFE-Loaded carbon on the catalyst layer of polymer electrolyte fuel cells. J Electrochem Soc 1995;142:4143–9. https://doi.org/10.1149/1.2048477.
[21] Uchida M. Effects of microstructure of carbon support in the catalyst layer on the performance of polymer-electrolyte fuel cells. J Electrochem Soc 1996;143:2245. https://doi.org/10.1149/1.1836988.
[22] von Sturm F. Carbon materials. Carbon—electrochemical and physicochemical properties. By K. Kinoshita. Wiley, New York 1988. Xiii, 533 pp., bound, £ 65.00.—ISBN 0-471-84802-6vol. 100; 1988. p. 1260–1. https://doi.org/10.1002/ange.19881000944. Angew. Chemie.
[23] Zhang J, Lima FHB, Shao MH, Sasaki K, Wang JX, Hanson J, Adzic RR. Platinum monolayer on nonnoble Metal–Noble metal Core–Shell nanoparticle electrocatalysts for O2 reduction. J Phys Chem B 2005;109:22701–4. https://doi.org/10.1021/jp055634c.
[24] Kinoshita K, Bett JAS. Potentiodynamic analysis of surface oxides on carbon blacks. Carbon N Y 1973;11:403–11. https://doi.org/10.1016/0008-6223(73)90080-8.
[25] Sobolyeva T. On the microstructure of pem fuel cell catalyst layers. Simon Fraser University; 2010.
[26] Salari S. Gas diffusion in thin porous catalyst layers of PEM fuel cells. Simon Fraser University; 2018.
[27] Uchida M, Aoyama Y, Eda N, Ohta A. New preparation method for polymer-electrolyte fuel-cells. J Electrochem Soc 1995;142:463–8. https://doi.org/10.1149/1.2044068.
[28] Ihonen J, Jaouen F, Lindbergh G, Lundblad A, Sundholm G. Investigation of mass-transport limitations in the solid polymer fuel cell cathode. J Electrochem Soc 2002;149:A448. https://doi.org/10.1149/1.1456917.
[29] Eikerling M, Andreaus B, Promislow K, Paddison S. Catalyst layer operation in PEM fuel cells: from structural pictures to tractable models. In: Mater. Model. PEM fuel cells. New York, NY: Springer; 2008. https://doi.org/10.1007/978-0-387-78691-9_3.
[30] Eikerling M. Water management in cathode catalyst layers of PEM fuel cells. J Electrochem Soc 2006;153:E58. https://doi.org/10.1149/1.2160435.
[31] Malek K, Eikerling M, Wang Q, Navessin T, Liu Z. Self-organization in catalyst layers of polymer electrolyte fuel cells. J Phys Chem C 2007;111:13627–34. https://doi.org/10.1021/jp072692k.
[32] Zhang X, Ostadi H, Jiang K, Chen R. Reliability of the spherical agglomerate models for catalyst layer in polymer electrolyte membrane fuel cells. Electrochim Acta 2014;133:475–83. https://doi.org/10.1016/j.electacta.2014.04.060.
[33] Salari S, McCague C, Tam M, Stumper J, Bahrami M. Modeling diffusivity in catalyst layer of a PEMFC based on a unit cell approach. In: 228th ECS Meet., phoenix; 2015. p. 50.
[34] Salari S, McCague C, Tam M, Saha M, Stumper J, Bahrami M. Accurate ex-situ measurements of PEM fuel cells catalyst layer dry diffusivity. ECS Trans 2015;69:419–29.
[35] Cheng B, Ni P, Jin C, Li Z, Zhang D, Dong P, Guo X. More direct evidence of the fcc arrangement for artificial opal. Optic Commun 1999;170:41–6. https://doi.org/10.1016/S0030-4018(99)00434-4.
[36] Inoue G, Kawase M. Effect of porous structure of catalyst layer on effective oxygen diffusion coefficient in polymer electrolyte fuel cell. J Power Sources 2016;327:1–10. https://doi.org/10.1016/J.JPOWSOUR.2016.07.037.
[37] Ellis AB. Teaching general chemistry: a materials Science companion. American Chemical Society; 1993. https://books.google.ca/books?id=igXwAAAAMAAJ.
[38] Voet A, Aboytes P. Porosity of carbon blacks. Carbon N. Y. 1971;9:135–8. https://doi.org/10.1016/0008-6223(71)90126-6.
[39] Bahrami M, Yovanovich MM, Culham JR. Pressure drop of fully-developed, laminar flow in microchannels of arbitrary cross-section. J Fluids Eng 2006;128:1036–44. https://doi.org/10.1115/1.2234786.
[40] Johnson KL, Johnson KL. Contact mechanics. Cambridge University Press; 1987. https://books.google.ca/books?id=Do6WQlUwbpkC.
[41] Walton K. The effective elastic moduli of a random packing of spheres. J Mech Phys Solids 1987;35:213–26. https://doi.org/10.1016/0022-5096(87)90036-6.
[42] Koiter WT. A spherical shell under point loads at its poles. BROWN UNIV PROVIDENCE RI DIV OF APPLIED MATHEMATICS; 1962.
[43] Taber L a. Large deflection of a fluid-filled spherical shell under a point load. J Appl Mech 1982;49:121. https://doi.org/10.1115/1.3161953.
[44] Zhou Y, Jiao K, Du Q, Yin Y, Li X. Gas diffusion layer deformation and its effect on the transport characteristics and performance of proton exchange membrane fuel cell. Int

J Hydrogen Energy 2013;38:12891–903. https://doi.org/10.1016/j.ijhydene.2013.05.150.

[45] Flückiger R, Freunberger SA, Kramer D, Wokaun A, Scherer GG, Büchi FN. Anisotropic, effective diffusivity of porous gas diffusion layer materials for PEFC. Electrochim Acta 2008;54:551–9. https://doi.org/10.1016/j.electacta.2008.07.034.

[46] Gigos PA, Faydi Y, Meyer Y. Mechanical characterization and analytical modeling of gas diffusion layers under cyclic compression. Int J Hydrogen Energy 2015;40:5958–65. https://doi.org/10.1016/j.ijhydene.2015.02.136.

[47] Xu G, LaManna JM, Clement JT, Mench MM. Direct measurement of through-plane thermal conductivity of partially saturated fuel cell diffusion media. J Power Sources 2014;256:212–9. https://doi.org/10.1016/j.jpowsour.2014.01.015.

[48] Jiao K, Park J, Li X. Experimental investigations on liquid water removal from the gas diffusion layer by reactant flow in a PEM fuel cell. Appl Energy 2010;87:2770–7. https://doi.org/10.1016/j.apenergy.2009.04.041.

[49] Feser JP, Prasad AK, Advani SG. Experimental characterization of in-plane permeability of gas diffusion layers. J Power Sources 2006;162:1226–31. https://doi.org/10.1016/j.jpowsour.2006.07.058.

[50] Khajeh-Hosseini-Dalasm N, Sasabe T, Tokumasu T, Pasaogullari U. Effects of polytetrafluoroethylene treatment and compression on gas diffusion layer microstructure using high-resolution X-ray computed tomography. J Power Sources 2014;266:213–21. https://doi.org/10.1016/J.JPOWSOUR.2014.05.004.

[51] Young RJ, Lovell PA. Introduction to polymers. 3rd ed. Third: CRC press; 2011. https://books.google.ca/books?id=ImQg2MK8NtkC.

[52] Malekian A, Salari S, Tam M, Oldknow K, Djilali N, Bahrami Majid. Compressive behaviour of thin catalyst layers. Part I - Experimental study. Int J Hydrogen Energy 2019;44:18450–60.